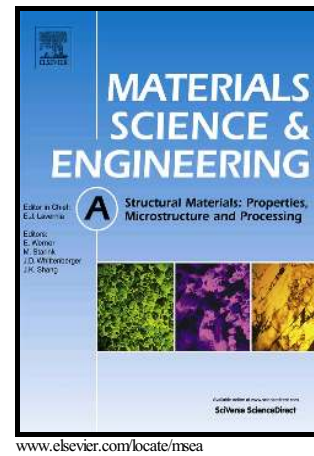# Author's Accepted Manuscript

Mechanical Properties and Microstructure of Laser Welded Ti–6Al–2Sn–4Zr–2Mo (Ti6242) Titanium Alloy

A. Chamanfar, T. Pasang, A. Ventura, W.Z. Misiolek

Mechanical Properties and Microstructure of Laser Welded Ti–6Al–2Sn–4Zr–2Mo (Ti6242) Titanium Alloy

A. Chamanfar [a*], T. Pasang [b], A. Ventura [a], and W.Z. Misiolek [a]

[a] Institute for Metal Forming, Department of Materials Science and Engineering, Lehigh University, 5 East Packer Avenue, Bethlehem, PA 18015, USA

[b] Department of Mechanical Engineering, Auckland University of Technology, Auckland, New Zealand

*Corresponding author. Tel.: +1 610 758 4218; Fax: +1 610 758 4244. E-mail address:

ahc215@lehigh.edu

Abstract

Room temperature tensile properties and microhardness of a laser welded Ti–6Al–2Sn–4Zr–2Mo (Ti6242) titanium alloy sheet were examined and correlated to the microstructure evolution across the weld. Tensile testing integrated with the optical image correlation Instron® system indicated that the average yield strength (YS), ultimate tensile strength (UTS), and total elongation of the weldment were respectively 88 %, 87 %, and 69 % of the corresponding base material (BM) values. Electron probe microanalysis (EPMA) demonstrated a uniform distribution of the main alloying elements across the weld. The hardness raised increasingly from the BM toward the heat affected zone (HAZ) and the fusion zone (FZ) due to mainly a higher α volume fraction in HAZ and acicular α' martensite formation in the FZ. Because of the higher hardness of the HAZ and FZ, a higher YS for the weldment relative to the BM would be expected. However, the lower YS as well as the lower UTS of the weldment can be explained by

1

presence of some porosity and underfill in the FZ. The lower total elongation of the weldment compared to the BM can be related to the higher hardness of the HAZ and FZ.

Keywords: Titanium alloy; laser welding; mechanical properties; microstructure; EPMA

1. Introduction

Ti6242 is a near-α titanium alloy used as the key structural components in the hot section of power generation and aircraft gas turbines as disks, impellers, and sheet metal components such as afterburner cans and hot airframes with a service temperature of up to 538 °C [1]. These applications require an excellent combination of high strength-to-weight ratio and adequate corrosion/oxidation resistance at room and elevated temperatures. The nominal chemical composition of the Ti6242 alloy by weight percent (wt. %) is: 6.20 Al, 1.95 Sn, 3.80 Zr, 2 Mo, 0.08 Si, 0.021 C, 0.008 N, 0.06 O, 0.0016 H, and balance Ti [2, 3]. The alloy has a bi-modal microstructure and consists of α and β phases with crystal structures of hexagonal close packed (HCP) and body centered cubic (BCC), respectively. The α to β transformation temperature or β-transus in Ti6242 is about 993 °C [4]. Al and interstitials (O, N, and C) are α stabilizer, *i.e.,* they raise the β-transus while Mo is β stabilizer [5]. In contrast, Zr and Sn have slight effect on β-transus but they strengthen the α phase by solid-solution strengthening mechanism [5]. The α phase has a higher strength and lower ductility compared to the β phase [4] and thus, is the main strengthening phase in this alloy. The oxidation and corrosion resistance of the alloy in different oxidizing/corrosive environments is supplied primarily by Ti, through formation of a protective TiO_2 oxide film [5].

As a result of the high reactivity of molten Ti with oxygen, hydrogen, and nitrogen leading to deterioration of mechanical properties of the weld metal, it is essential to perform the

2

welding under protective inert gas or vacuum environment. Accordingly, advanced fusion welding techniques such as laser and electron beam welding have been extensively employed to join or repair various titanium alloy components used in gas turbines. Specifically, laser welding is attractive for welding of difficult-to-join Ti alloys because this welding technology provides high welding speed, high energy density, low heat-input, a narrow FZ and HAZ, low distortion, low residual stresses, and ease of automation [6, 7].

In general, welding of Ti alloys can be associated with some metallurgical problems. For instance in gas tungsten arc welded Ti–6Al–2Sn–4Zr–6Mo(Ti6246), the elongation of the weld metal is reported to be 0.4 % [8]. This weld brittleness is related to the formation of brittle phases (*e.g.,* formation of extremely fine lamellar α phase), precipitation of hard and brittle particles and formation of hydrides in the weld metal [6, 9, 10]. The post-weld heat treatment (PWHT) can slightly improve the ductility in brittle Ti alloy welds [8]. Similarly, in laser welded Ti–6Al–4V (Ti64), an $\alpha + \beta$ titanium alloy, it is reported that the hardness in the FZ is 140 HV higher than that of the BM [11]. This increase in the FZ hardness is related to the formation of α' (martensite) due to the high cooling rates upon weld metal solidification [9, 11]. Furthermore, loss of alloying elements in the weld metal due to evaporation is another issue in welding of Ti alloys. For instance, in electron beam welded Ti–5Al–5V–5Mo–3Cr (Ti–5553), the Al content was reduced to 4.66 wt. % from the BM value of 4.95 wt. % [9].

As discussed above, the mechanical property and microstructure of several laser or electron beam welded Ti alloys such as Ti64 [11], Ti5553 [9], and Ti–6.5Al–3.5Mo–1.5Zr–0.3Si [12] have been well investigated and reported in the literature. However, little data are available in literature on the microstructure and mechanical properties of laser welded Ti6242 and even

3

less on the variation in the chemical composition across the weld. Accordingly, this study has been undertaken to map variation in mechanical properties, microstructure, and chemical composition across the weld in laser welded Ti6242. Such investigation will provide key data which will be useful for maximizing the integrity of the laser welded Ti6242.

2. Experimental Material and Procedures

Rectangular bars of Ti6242 with dimensions of 160 mm × 76 mm × 76 mm (length × width × thickness) were received. The bars were forged and subsequently annealed at temperatures below the β-transus by the manufacturer. The bars were sliced into 1.6 mm thick sheets along the length × width plane by wire electro-discharge machining (EDM). To remove any previous oxides and/or surface contaminations that may adversely affect the integrity of the weldments, the surfaces to be welded were brushed and then cleaned with ethanol. The sheets were then laser welded autogenously at a power of 3 kW, Argon gas shielding of 20 to 30 L/min, and travelling speed of 100 mm/sec. To examine the integrity of the laser welded Ti6242 by tensile testing, as schematically illustrated in Fig. 1, three subsize ASTM E8 flat dog-bone tensile samples were extracted from the laser welded sheets transverse to the weld line in the as-welded condition by wire EDM. It is noteworthy that the weld line was located in the middle of the gage length in the flat tensile samples. The EDM can generate a recast layer on the surface of tensile samples which can lead to premature failure during tensile loading. Therefore, prior to tensile testing the tensile gage section was ground using 800-grit SiC paper.

For tensile testing, the tensile axis was perpendicular to the weld line. Tensile tests were carried out at room temperature based on the ASTM E8-13a standard at an initial strain rate of 3×10^{-3} s^{-1} using a 30 kN Instron 5567 universal tensile testing machine integrated with an Instron® digital image correlation system. The latter is a non-contact optical system that captures real-time images during tensile testing to determine the elongation distribution for every deformation stage. The system uses a CCD camera capable of capturing 50 frames per second (fps) and needs a speckle pattern consisting of white dots randomly sprayed on the grey flat surface of the gage length in the tensile sample. In this study 2 fps was used during testing and

4

the analysis of the captured images were performed by the Instron® dedicated software to obtain the elongation distribution for each deformation step.

In addition to mapping the elongation distribution, this Instron® digital imaging system is also capable to work at the same time as an optical extensometer. To this end, prior to tensile testing, in addition to the speckle pattern, two larger white dots were marked on the same side of the tensile sample to distinguish the gage region (32 mm) by the optical extensometer during tensile testing. To attain the stress-strain curves and the related tensile properties (YS, UTS, and total elongation), the load data, recorded by the tensile testing machine, were used to calculate the engineering stress, while the elongation was determined from the data recorded by the optical extensometer. In order to compare the tensile properties of the weldments with those of the BM, tensile samples with the same geometry were prepared from the as-received BM Ti6242 sheet by wire EDM and then tensile tested under the same conditions as the weldments.

To map the variation in the chemical composition, measure the microhardness, and characterize the microstructure, further sections through a plane perpendicular to the weld line (Fig. 1) were prepared from the welded sheets by wire EDM. At the initial stages of this study, it was found that metallographic sample preparation for the welded Ti6242 alloy was challenging; however, an effective metallography procedure was developed for this alloy. The details of this procedure are provided in Table 1. For grinding, 320 and 600 SiC papers were respectively used. After grinding, the samples were polished on a low nap cloth for one minute using 6 μm diamond suspension polishing solution. The polishing was continued for another one minute using a high nap cloth and 1 μm aluminum oxide polishing solution. Subsequent polishing was performed using a medium nap cloth and 0.3 μm aluminum oxide for 2 minutes. Final polishing of the samples was carried out on a medium nap cloth for 2 minutes using 0.05 μm silicon dioxide polishing solution. After each grinding/polishing step, the sample surface was cleaned with cotton and water, and then flushed with ethanol and finally dried. The developed metallography procedure was used to prepare the hot mounted metallographic samples for mapping chemical composition variation, microhardness testing, and microstructural examination across the weld. To examine the variation in the chemical composition across the weld, EPMA was performed on the as-polished samples using a JEOL 733 SuperProbe operated at 10 kV and 50 nA. For EPMA the weld-cross section was scanned at the mid-thickness as shown in Fig. 2.

To assess variation in the mechanical properties across the weld, Vickers microhardness measurement was carried out on the as-polished samples with a surface finish of 0.05 μm under a load of 300 g and a dwell time of 13 s using a Leco® Microhardness Tester LM248AT with a Vickers diamond pyramid indenter. The microhardness measurements extended from FZ to HAZ and BM on both sides. Microhardness was determined on three lines spaced ~ 415 μm along the sheet thickness as shown in Fig. 2. Also, along each line in the x direction (Fig. 2) the distance between each indent was 200 μm, *i.e.,* at least five times the indent diameter (40 μm on average). In total 30 hardness measurements were executed on each line and the results for each line is reported in this study.

To reveal the microstructure of the different zones by optical microscopy, the as-polished samples were immersion etched for five seconds in Kroll's reagent composed of 3 mL HF, 6 mL

HNO$_3$, and 100 mL H$_2$O. The volume fraction of the primary α phase across the weld was determined according to the point counting method described in the ASTM E 562-02 standard. Moreover, the equivalent diameters of the primary α and the transformed β across the weld were measured using the Clemex® image analysis software and reported as their corresponding sizes in this study. For volume fraction determination and size measurements at least five micrographs were considered for each region of interest across the weld. For size measurements, on each image at least 10 primary α and 10 transformed β were sampled.

To determine the fracture mode and relate it to the mechanical properties of the weldments, fractography studies following tensile testing were carried out. To this end, the fracture surface of the tensile samples was examined under a Hitachi S-4300 scanning electron microscope (SEM) operated at 15 kV in the secondary electron mode.

3. Results and Discussion

3.1. Average Tensile Properties

In this study, the integrity of the laser welded Ti6242 was investigated by tensile testing. For the as-laser welded Ti6242, the average tensile properties of the weld are tabulated in Table 2 and plotted in Fig. 3. In Table 2 and Fig. 3, each datum point (YS, UTS and total elongation) for weldment is the average of the corresponding tensile property values determined for the three dog-bone tensile samples extracted from the laser welded sheet. As a point of reference, the tensile properties of the BM in the as-received condition are also provided in Table 2 and Fig. 3. The obtained tensile properties for the BM were very close to those reported in Reference [13] as can be observed from Table 2. This indicates the reliability of the tensile testing procedure used in this study. It is noteworthy that the YS was measured at a point where deviation from a linear behavior was observed. Also, the error bars in Table 2 are the standard deviations of the tensile properties for the tensile samples.

Analysis of the results indicated that the average YS, UTS, and total elongation (shown by the right hand abscissa in Fig. 3) of the weldment were respectively 88 %, 87 %, and 69 % of the BM corresponding values. Of interest in this analysis of the mechanical performance of the as-laser welded Ti6242 was also the standard deviation in the tensile properties. The standard deviations of YS and UTS were negligible (below 1 %) as can be observed from Table 2. Also,

the standard deviation in the total elongation (6 %) was not significant and remained in the range of experimental scatter in the data. The basis for the consistency in the mechanical performance of the as-laser welded Ti6242 is discussed next.

3.2. Tensile Properties along the Weld Line

Figure 4 illustrates the tensile properties of the individual samples extracted according to Fig. 1 from the as-laser welded Ti6242 sheet. It is noteworthy that the corresponding tensile properties of the BM in the as-received condition are depicted as horizontal lines for reference. For the YS and UTS (Fig. 4a and b), the individual values for each of the three tensile samples were relatively uniform. Therefore, uniform YS and UTS along the weld line explains negligible standard deviation in the average YS and UTS (Table 2). By contrast, for the total elongation, the value for the third sample (12.5 %) was slightly lower than those of tensile samples 1 and 2 (respectively 13.4 % and 14.2 %). This slight difference in the elongation along the weld line have resulted in a slightly higher standard deviation in the average elongation (Table 2) compared to the average YS and UTS. The characteristics of the FZ and HAZ affect the mechanical performance, which is discussed in Sections 3.4 to 3.6.

A typical stress-strain curve for the individual samples extracted from the laser welded Ti6242 sheet is compared with that of the BM in Fig. 5. The elastic and plastic behaviors of the weld tensile sample are different from those of the BM. This difference can be related to the characteristics of the FZ and HAZ (width, hardness, and microstructure) that will be discussed in Sections 3.4 to 3.6. However, the area under the stress-strain curves which represents the toughness was calculated for the weld and the BM. It was found that the average toughness of the weldment, *i.e.,* $(11783 \pm 544) \times 10^4$ J/m^3, was lower than the BM value, *i.e.* $(20224) \times 10^4$ J/m^3. In other words, the weldment exhibited a toughness 58 % of the BM value. The failure location during tensile testing of the individual samples (Fig. 1) extracted from the laser welded Ti6242 sheet is reported in Table 2. For samples 1 and 3 failure occurred in the FZ. For sample 2, tensile failure occurred exclusively in the BM.

3.3. Variation in the Chemical Composition across the Weld

The results of the EPMA analysis performed for the major alloying elements in Ti6242 weld are presented in Fig. 6. In the EPMA analysis two approaches were followed. First, as schematically presented in Fig. 6a, chemical analysis was carried out across the weld using a probe or beam size of 2 μm and a step size of 20 μm in the FZ and 50 μm in the HAZ and BM. It can be observed that the distribution of the major alloying elements, *i.e.* Al, Zr, Sn, and Mo, in the FZ is relatively uniform. This can be related to the fine and uniform α' martensitic microstructure in the FZ as described in Section 3.5. By contrast, for Al, Zr, and Mo there are fluctuation in the distribution of these alloying elements in the HAZ and BM regions. This can be explained in terms of presence of α and β phases in the HAZ and BM as will be explained in Section 3.5. Indeed, due to a small beam size (2 μm) and coarser α and β sizes (*e.g.,* 13.5 ± 4.8 μm and 18.0 ± 6.2 μm respectively for BM), depending on whether the measurement location was on α or β phase, a different chemical composition was read as these alloying elements have different affinity for α and β phases. Interestingly, for Sn the chemical concentration from FZ to BM is relatively uniform indicating that Sn has an almost equal affinity for α and β phases. Also, by determining the average concentration of Al, Mo, and Zr for the BM and plotting the data as a horizontal line, it can be observed that the chemical concentration of Al, Mo, and Zr in the FZ is very close to the BM corresponding average value (Fig. 6b). Also, in HAZ the *average* chemical concentration of Al, Mo, and Zr is not significantly different from the BM corresponding average value. This analysis indicates that variation in the chemical composition across the weld for major alloying elements is not significant in laser welded Ti6242.

In the second EPMA analysis or approach, as schematically presented in Fig. 6a, a larger beam size (20 μm) was used and measurements were carried out for different ten locations in HAZ as well as in the BM. With this beam size it was expected that for each measurement spot in BM and HAZ, both α and β phases at least partially were included in the analysis, and thus, more average representative results can be obtained. To have even a better characteristic analysis, as shown schematically in Fig. 6a, the average of the ten measurements in HAZ as well as the BM were determined and reported in Fig. 6c. Again, it can be observed that the

9

distribution of Al, Zr, Sn, and Mo from FZ to BM is uniform. This is a sign of a sound weld since losing alloying elements during welding in the FZ due to evaporation is not desirable.

For Si which is a minor element in Ti6242, the concentration was scattered in the 0.08 to 0.12 wt. % range in the FZ, HAZ, as well as BM. Of interest in this analysis is the standard deviation in the chemical analysis in HAZ and BM (Fig. 6c). For Sn which has almost equal affinity for α and β phases, the standard deviation in the measurements presented as error bar was negligible, *i.e.,* less than the marker size. In contrast, for Zr, Al, and Mo which have progressive affinity in partitioning either in α or β phases, the standard deviation in concentration of Zr, Al, and Mo progressively increased.

3.4. Microhardness Evolution

In order to map the variation in the mechanical properties across the weld, microhardness measurements were carried out. The variation in the microhardness across the weld in laser-welded Ti6242 for three hardness lines (Fig. 2) is plotted in Fig. 7 for the as-welded condition. For the BM, the hardness varies from 303 to 363 HV. This variation can be related to the indent size and α/β size. The average indent diameter was 40 μm while α and β had the respective size of 13.5 ± 4.8 μm and 18.0 ± 6.2 μm in the BM. Therefore, hardness can be measured either mostly on the β phase, or partly on α and partly on β. Since β is softer and more ductile than α, there will be variation in the measured hardness of the BM. In contrast, in the FZ the microstructure was uniform and finer as demonstrated in Section 3.5. Therefore, there is a lower degree of scatter in the microhardness data for FZ. The HAZ region can be divided into two subregions, *i.e.,* A and B, as shown on microhardness profile and further discussed in Section 3.5. For both of these regions of HAZ, although the microstructures are to some extent different from each other, they are finer compared to the BM (Section 3.5). Hence, for each region the hardness data are less scattered compared to the BM.

According to Fig. 7, by moving from the BM toward the HAZ and FZ the hardness increases for all the three hardness profiles. In FZ either a single peak or a small kink in the hardness peak leading two smaller hardness peaks was observed for the three hardness lines. Also, the variation in the hardness in the FZ is not significant. Moreover, although measured from different locations along the sheet thickness (Fig. 2), similar hardness profiles were found

10

for the three hardness lines. Also, almost a symmetric hardness profile was observed for the two sides of the weld centerline. The observed symmetry in the microhardness profiles with respect to the weld centerline indicates that the two weld part are affected thermally almost in the same way.

The variation in the *average* hardness from BM to FZ is presented in Fig. 8. The best fit to the data is also depicted as a dotted curve. It can be seen that hardness continuously increases from BM (329 ±13 HV) to HAZ (B: 334 ± 10 and A: 391 ±4 HV) and FZ (435 ± 6 HV). The average hardness in subregion A of HAZ is 1.2 times the BM average hardness value. Similarly, the average hardness in FZ is 1.3 times the BM average hardness value. It is noteworthy that due to fluctuation in the BM hardness values (Fig. 7), the standard deviation of the BM average hardness is higher compared to those of the HAZ and FZ where a more consistent hardness was measured. The contribution of the microstructural features to the observed microhardness behavior will be discussed in the next section.

3.5. Microstructure Observation across the Weld

Overall Weld Geometry and Defects: A low magnification EPMA image of the laser welded Ti6242 is presented in Fig. 2. Three distinct zones, namely FZ, HAZ, and BM can be identified from the contrast and microstructure. The FZ is narrower at the middle and wider in the top and bottom regions. The FZ is 466 ± 11 μm wide at the middle. As marked on Fig. 2 some metallurgical defects such underfill and gas porosity (also known as solidification pores) can be observed in the FZ. Loss of material from the top surface due to evaporation and expulsion of the molten metal is most probably the major cause for the development of the underfill defect during laser welding of Ti6242 [14]. Also, rapid cooling of the FZ can lead to inadequate filling of the weld gap and thus promote formation of the underfill defect at the top [15]. Based on the AWS D17-1 standard, the maximum allowable underfill depth is 7 % of the sheet thickness, *i.e.,* 112 μm for the current Ti6242 laser welded sheet. The maximum depth of the underfill in the current Ti6242 laser weld was determined to be 65 μm which is within the allowable limit of the AWS D17-1 standard.

It is well known that porosity is formed in the FZ due to entrapment of gas bubbles that cannot escape before solidification. In titanium welds, hydrogen is reported to be the main source

for generation of the gas porosity [16]. Contamination of the weld parts by grease, oil, and dirt can supply hydrogen for gas porosity formation. Similar to this work, the presence of underfill and porosity in the FZ has been observed for laser welded Ti64 [14] and Ti5553 [9, 17]. As discussed in Section 3.6, the presence of underfill and porosity in the FZ of laser welded Ti6242 can affect the tensile properties.

Referring back to Fig. 2, a part of HAZ has a brighter contrast compared to the FZ and BM. The overall HAZ is 460 ± 9 μm wide at the middle on either side of the FZ determined based on the microstructure studies detailed below as well as microhardness measurements. It can be observed that laser welding generates a narrow FZ and HAZ. The microstructures of BM, HAZ, and FZ at higher magnifications are presented in Fig. 9.

BM Microstructure: For the BM Ti6242 a combination of equiaxed and lamellar microstructure was observed. In other words, the BM has a near α bimodal or duplex microstructure which consists of equiaxed primary α grains (α_p: bright phase in Fig. 9a and b) distributed in a matrix of transformed β phase (dark phase in Fig. 9a and b). The transformed β phase is indeed a lamellar $\alpha + \beta$ constituent composed of fine acicular α phase in the β matrix (or in another word alternate layers of α and β phases), as shown at higher magnification in Fig. 9b. For better understanding of the BM microstructure, the location of the Ti6242 in a pseudobinary Ti phase diagram is presented in Fig. 10. Usually, Ti6242 is hot deformed in the $\alpha + \beta$ phase field (*e.g.,* at 930 °C) followed by air cooling [18]. Subsequently, the alloy is annealed in the $\alpha + \beta$ phase field (*e.g.,* at 955 °C for 1 h) to attain a considerable volume fraction of equiaxed primary α grains [18]. Upon cooling from the hot deformation/annealing temperature, α begins to nucleate at the β grain boundaries and grows as a lamellar phase into the prior β grains. In fact, the α plates form with their close-packed (basal) plane parallel to a distinct plane in the β matrix [19]. Due to a near atomic matching along this common plane, the α phase grows faster along this plane but thickens rather sluggishly transverse to this plane [19]. By this means, α plates or layers are generated in the β matrix. The α that forms by this mechanism is known as secondary α or α_s. The resulting microstructure is a distribution of primary α grains and a transformed β matrix where the latter is actually composed of α and β lamellas with a random orientation (Fig. 9b). The volume fraction of the primary α in the BM Ti6242 was determined to be 36 ± 1 %.

12

Also, the sizes of the primary α and the transformed β in the BM were 13.5 ± 4.8 µm and 18.0 ± 6.2 µm, respectively.

This type of BM microstructure provides the balanced mechanical properties for the Ti6242 alloy. The equiaxed microstructure supplies high ductility and high fatigue resistance while the lamellar microstructure provides high fracture toughness, excellent creep resistance, and fatigue crack growth resistance [3]. The latter can be related to the deflection of the propagating fatigue cracks along various randomly oriented lamellae [3].

During laser welding the material is heated to temperatures significantly higher than the β-transus temperature and cooled down at a very high cooling rates. As the laser source travels away, the heat input in the melting pool and HAZ dissipates into the nearby regions quickly leading to rapid cooling of the FZ and HAZ. Therefore, the microstructures of the HAZ and FZ are expected to be significantly different from that of the BM.

HAZ Microstructure: According to HAZ microstructure (Fig. 9c), there are two distinct subregions in the HAZ: one which has been exposed to temperatures higher than the β-transus temperature (subregion A in Fig. 9c: 160 ± 7 µm wide) and one which has experienced temperatures mostly in the $\alpha + \beta$ domain (subregion B in Fig. 9c: 300 ± 10 µm wide). In subregion A, the area adjacent to the weld metal pool or more precisely close to the solid-liquid interface, the temperature has apparently exceeded the β-transus temperature (993 °C) during laser welding. Therefore, the primary α phase and the lamellar $\alpha + \beta$ constituent would all transform into the single β phase according to the phase diagram presented in Fig. 10. Upon cooling from this single phase β domain, abundant primary α nucleates and grows rapidly as a result of the fast cooling rate and significant degree of under cooling. Thus, the volume fraction of the primary α phase would be higher in the subregion A of HAZ compared to the BM as illustrated in Fig. 11a. The rest of the HAZ (subregion B) was heated high enough in the $\alpha + \beta$ domain to cause a slight decrease in the primary α volume fraction (Fig. 11a) compared to that of the BM. This can be attributed to the fact that during the heating cycle of the laser welding, the volume fraction of the primary α phase in subregion B of HAZ decreases according to the phase diagram presented in Fig. 10. On the other hand, upon the cooling phase of the laser welding, subregion B of HAZ experiences higher cooling rates compared to subregion A as the former is close to the cooler BM while the latter is in contact with hot weld metal. As a result,

13

the microstructure in subregion B is somehow similar to a microstructure quenched from the $\alpha + \beta$ domain. Since transformed β phase is the counterpart of the primary α phase, the reverse situation exists for the evolution of the transformed β volume fraction in the BM and HAZ compared to that of the primary α.

The primary α size in these two subregions of the HAZ is compared to that of the BM in Fig. 11b. There is no significant difference in the size of the primary α phase for the investigated locations. Due to a higher cooling rate in subregion A of HAZ compared to that of the BM through industrial manufacturing, *i.e.,* forging and annealing, the primary α size in subregion A of HAZ may be expected to be slightly smaller relative to the BM. This difference in the cooling rate can be related partly to the smaller thickness of the laser welded sheet compared to the bar from which BM was extracted and partly to thermal cycles in laser welding and BM manufacturing. However, due to the presence of the fine and coarse/agglomerated primary α in these regions leading to considerable standard deviation in the primary α size in the BM and HAZ, this difference is not reflected in the measurements.

The variation in the transformed β size for BM and HAZ is shown in Fig. 12. The β phase in subregion A of HAZ is finer compared to the BM. This can be related to transformation of the lamellar $\alpha + \beta$ constituent (transformed β) to the single β phase during heating cycle of laser welding due to experiencing temperatures over the β-transus (993 °C), and formation of a finer β upon cooling cycle of the laser welding. Also, since primary α are normally formed at the prior β grain boundaries, the increase in the volume fraction of the primary α in subregion A of HAZ compared to the BM leads to a finer β in this subregion relative to the BM. Slightly finer β in subregion B of HAZ compared to subregion A can be attributed to higher cooling rate in the former as discussed above. Again, the considerable standard deviation in the β size in the BM and HAZ is caused by presence of fine and coarse β in these regions.

A higher volume fraction of the primary α phase in subregion A of HAZ results in a higher hardness in this subregion (Fig. 8) compared to the BM and subregion B of HAZ as α is harder than β. Also, finer transformed β in subregion A of HAZ compared to the BM contributes to the increase in the hardness. The hardness in subregion B of HAZ is slightly higher than that of the average BM hardness due to slightly finer transformed β.

In the areas far from the melting pool, *i.e.,* the BM, the temperature during laser welding remains below the transformation temperatures and thus, the bimodal microstructure of the BM was not affected.

FZ Microstructure: based on the time-temperature-transformation (TTT) diagram provided by Donachie [4], the critical cooling rate for attaining a fully *α'* martensitic microstructure in Ti6242 can be estimated as 1303 °C/s. Also, the start temperature for *α'* martensite formation in Ti6242 alloy is 800 °C. Additionally, according to Li *et al.* [20], the average cooling rate during laser welding from very high temperatures to 800 °C in the FZ can be estimated to be at least 1510 °C/s. Such a cooling rate is significantly higher that the critical cooling rate necessary for *α'* martensitic formation in Ti6242. Therefore, as the weld metal cools down, the single *β* phase forms from the molten metal. Since the FZ experiences very rapid cooling during the solidification process especially in this thin laser welded Ti6242 sheet (1.6 mm thick), an acicular *α'* martensitic microstructure is formed in the FZ of the as-welded Ti6242 (Fig. 9e and f) as a result of the rapid cooling of the columnar *β* grains. Formation of the acicular *α'* martensite with an HCP crystal structure in the FZ results in the average microhardness of the FZ to be 108 HV higher than that of the BM (Fig. 8).

3.6. Factors Contributing to the Mechanical Properties

According to Table 2, the average YS, UTS, and total elongation of the weldment were respectively 88 %, 87 %, and 69 % of the BM corresponding values. The tensile properties of the weldment are a combination of those of the FZ, HAZ, and BM. Since the hardness in the HAZ and FZ are higher than that of the BM (Fig. 8), it is expected that the weldment exhibits a higher YS compared to the BM. However, from one aspect, the length of the FZ and HAZ together (926 µm) comprises only 3 % of the tensile sample reduced length, *i.e.,* 32 mm. Even with this small contribution of the FZ and HAZ to the YS, the YS of the weldment at least should be equal to that of the BM since 97 % of the tensile sample reduced section length consists of the BM and the rest is FZ+HAZ with a higher hardness compared to the BM. However, the presence of some porosity as well as under fill in the FZ (Fig. 2) has resulted in a relatively lower YS in the weldment compared to the BM. Porosity and underfill decrease the cross-sectional area through thickness in the FZ, which can result in local stress concentration and decrease the YS and

fatigue strength of the weld [21]. Such a presence can also contribute to a lower UTS as well as a different elastic behavior in weldments compared to BM as can be observed from Fig. 5.

The lower elongation of the weldment compared to the BM can be related to the lower elongation of the HAZ and FZ due to a less ductile (harder) material in these regions. An elongation map of the tensile sample 1 at the final stages of the tensile test (just before fracture) is presented in Fig. 13. The gradients in color (or shading) specifies different elongation before fracture. It can be observed that the total elongation of the FZ and a portion of the HAZ remains below 4 %, the pink central area in Fig. 13, due to less ductile material in these regions. The maximum length of this pink central area is 8 % of the tensile sample reduced length (gage length) in Fig. 13. In the BM area of the weldment, *i.e.,* entire area of the gage section except the pink central area, the ductility of the material is much better. However, since the total elongation measured along the gage length includes those of the FZ, HAZ and BM as demonstrated previously [22, 23], due to lower elongation in the FZ and HAZ, the average total elongation of the weldment (13.4 %) is lower than that of the BM (19.4 %). In spite of porosity and underfill presence in the FZ (Fig. 2), deformation localization in the FZ is the lowest. This indicates that the martensitic structure in the FZ and a higher volume fraction of the primary α phase in the HAZ (subregion A) supply strengthening, though at the expense of the ductility. Consequently, the strengthening effect of the microstructures in the FZ and HAZ compensates for any weakening originating from presence of underfill and porosity.

3.7. Fractography

As was discussed in Section 3.2, for tensile samples 1 and 3 tensile fractured occurred in the FZ whereas for tensile sample 2 fracture occurred in the BM. The fractography SEM images of the tensile samples 2 and 3 are presented respectively in Figs. 14 and 15. It can be observed that depending on the fracture location, *i.e.,* FZ or BM, the fracture surface exhibits different features. An overview of the fracture surface of the tensile sample 2 is presented in Fig. 14a, b, and c. Higher magnification images of the circled areas in Fig. 14b and c are shown in Fig. 14d, e, f, g, and h. According to Fig. 14a, b, and c in tensile sample 2 with fracture in the BM, the fracture surface can be divided into two regions: (i) smoother topographic fracture surface located mostly in the surrounding of the fracture surface and (ii) central uneven topographic fracture surface. For both regions, the primary fracture mechanism is microvoid coalescence

16

leading to a dimpled rupture or final transgranular ductile fracture. However, for region (i) the microvoids are finer compared to region (ii). For both regions, some transgranular cleavage facets (cleavage planes) and tear ridges are also visible. A few cracks can also be observed in both regions.

It is well-known that the microvoids from which ductile fracture originates are initiated at locations where there is deformation incompatibility. In particular, strain hardening of two different phases (α and β in the BM) is different and incompatible. Therefore, interface between α and β can be the preferential nucleation sites for the microvoids formation.

An overview of the fracture surface of the tensile sample 3 with fracture in the FZ is presented in Fig. 15a, b, c, and d. Higher magnification images of the circled areas in Fig. 15a, b and d are shown in Fig. 15 e, f, g, and h. Compared to tensile sample 2, for tensile sample 3, many pores generated during laser welding can be observed. Indeed, these pores divide the fracture surface into two regions: (1) uneven topographic fracture surface containing numerous pores and (2) smoother topographic fracture surface with less porosity. Regions (1) and (2) are respectively located in the left and right side of the fracture surface. For region (1), the fine dimples presenting the transgranular ductile fracture are associated with large pores, Fig. 15f. In region (2) for which three representative areas are circled as e, g, and h in Fig. 15a to c and shown at higher magnification in Fig. 15e, g, and h, respectively, many finer dimples indicating microscopic ductility and thus, ductile fracture are visible. A few cracks, tear ridges, and transgranular cleavage facets can also be observed for both (1) and (2) regions. Comparing Fig. 14 and 15 would suggest finer dimples in the FZ relative to the BM which is consistent with the fine α' microstructure of the FZ (Fig. 9). In summary, consistent with the considerable elongation of the weldments (13.4 %, Table 2), a ductile fracture behavior for laser welded Ti6242 was observed as supported by Figs. 14 and 15.

4. Conclusions

The quality of the laser welded Ti–6Al–2Sn–4Zr–2Mo (Ti6242) titanium alloy sheet in terms of tensile properties, microhardness, chemical composition distribution, presence of defects, and microstructure in the as-welded condition was investigated. From this study the following conclusions can be drawn:

17

1. The average yield strength (YS), ultimate tensile strength (UTS), and elongation at failure of the weldments were respectively 88 %, 87 %, and 69 % of the base material (BM) corresponding values. Also, the area under the tensile stress-strain curves, which represents the toughness, was smaller (58 %) for laser welded Ti6242 compared to the BM.

2. Ductile fracture of the tensile samples occurred either in the BM or fusion zone (FZ) as a result of transgranular microvoid coalescence. The presence of porosity and underfill in the FZ as well as higher hardness (lower ductility) in the FZ and heat affected zone (HAZ) compared to the BM contributed to the observed tensile properties. The impact of the former was more pronounced on YS and UTS, and the latter on elongation.

3. For the BM Ti6242 a near α bimodal microstructure consisting of equiaxed primary α grains distributed in a matrix of transformed β containing fine acicular α was observed. Rapid solidification of the weld pool led to the formation of the acicular α' martensite and thus, an 108 HV increase in the average microhardness of the FZ compared to the BM average value (328 HV).

4. Due to exposure to high temperatures, the volume fraction of the primary α phase increased in a portion of HAZ leading to a 62 HV increase in the average microhardness relative to the BM.

5. According to electron probe microanalysis (EPMA), the distribution of the major alloying element, *i.e.,* Al, Zr, Sn, and Mo, from the FZ to the BM was uniform.

Acknowledgments

References

[1] 6242 Titanium Material Property Data Sheet: http://www.suppliersonline.com/propertypages/6-2-4-2-.1.asp, (2015).
[2] C. Quesne, Journal of the Less-Commun Metals, 68 (1979) 133-142.

[3] B. Sefer, Ph.D. Thesis, Division of Materials Science, Department of Engineering Sciences and Mathematics, Luleå University of Technology, Sweden, 2014.

[4] M.J. Donachie, Titanium, A Technical Guide, 2nd ed., ASM International, 2000.

[5] Titanum Alloy Guide, An RTI International Metals, Inc. Company, (2015).

[6] C. Ferdinand, J. Alexis, T. Masri, J.-A. Petit, J.-C. Ganza, 11th World Conference on Titanium, Kyoto, Japan, 2007

[7] M. Pang, G. Yu, H.-H. Wang, C.-Y. Zheng, Journal of Materials Processing Technology, 207 (2008) 271–275.

[8] F.D. Mullins, D.W. Becker, Welding Research Supplement, June (1980) 177-182.

[9] J.C. Sabol, T. Pasang, W.Z. Misiolek, J.C. Williams, Journal of Materials Processing Technology, 212 (2012) 2380-2385.

[10] J.C. Sabol, C.J. Marvel, M. Watanabe, T. Pasang, W.Z. Misiolek, Scripta Materialia, 92 (2014) 15–18.

[11] E. Akman, A. Demir, T. Canel, T. Sinmazcelik, Journal of Materials Processing Technology, 209 (2009) 3705–3713.

[12] Y. Zhu, J. Li, X. Tian, H. Wang, D. Liu, Materials Science and Engineering A, 607 (2014) 427-434.

[13] Technical Data Sheet: Timetal 6-2-4-2, Timet Metals Corporation, 2015.

[14] A.S.H. Kabir, X. Cao, J. Gholipour, P. Wanjara, J. Cuddy, A. Birur, M. Medraj, Metallurgical and Materials Transactions A, 43A (2012) 4171-4184.

[15] M. Pastor, H. Zhao, R.P. Martukanitz, T. DebRoy, Welding Journal, 78 (1999) 207s–216s.

[16] Z. Khaled, Journal of Materials Engineering and Performance, 3 (1994) 419–434.

[17] T. Shariff, X. Cao, R.R. Chromik, P. Wanjara, J. Cuddy, A. Birur, Journal of Materials Science, 47 (2012) 866–875.

[18] M. Benedetti, Fatigue and Fracture of Engineering Materials and Structures, 28 (2005) 909-922.

[19] J. Huang, Ph.D. Thesis, School of Metallurgy and Materials, The University of Birmingham, Birmingham, UK, 2011.

[20] Z. Li, S.L. Gobbi, F. Bonollo, A. Tiziani, G. Fontana, Science and Technology of Welding and Joining, 3 (1998) 1-7.

[21] J.C. Ion, Laser processing of engineering materials: principles, procedure and industrial application, Elsevier Butterworth-Heinemann, Oxford, UK, 2005.

[22] A. Chamanfar, M. Jahazi, J. Gholipour, P. Wanjara, S. Yue, Materials Science and Engineering A, 555 (2012) 117-130.

[23] A. Chamanfar, M. Jahazi, J. Gholipour, P. Wanjara, S. Yue, Materials Characterization 104 (2015) 149–161.

Fig. 1. Schematic presenting the geometry of the laser welded Ti6242 sheet, locations of the tensile samples as well as the sample for metallurgical characterization.
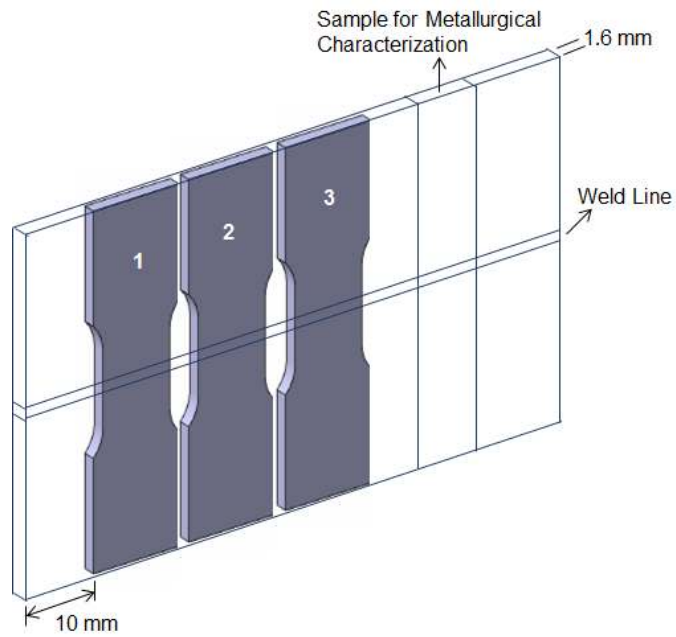
Fig. 1. Schematic presenting the geometry of the laser welded Ti6242 sheet, locations of the tensile samples as well as the sample for metallurgical characterization.

Fig. 2. An overview of the FZ geometry, size of the HAZ, EPMA scanning line, microhardness measurement along three lines, and the negative (- x) and positive (+ x) distances from the weld centerline for microhardness measurements.

20
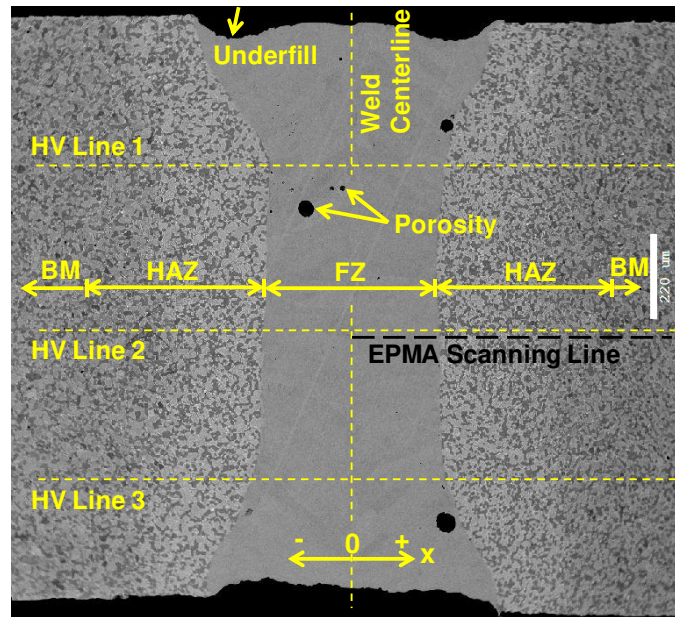
Fig. 2. An overview of the FZ geometry, size of the HAZ, EPMA scanning line, microhardness measurement along three lines, and the negative (- x) and positive (+ x) distances from the weld centerline for microhardness measurements.

Fig. 3. Average YS, UTS, and total elongation (right hand side vertical axis) of the as-laser welded Ti6242 compared to those of the BM.
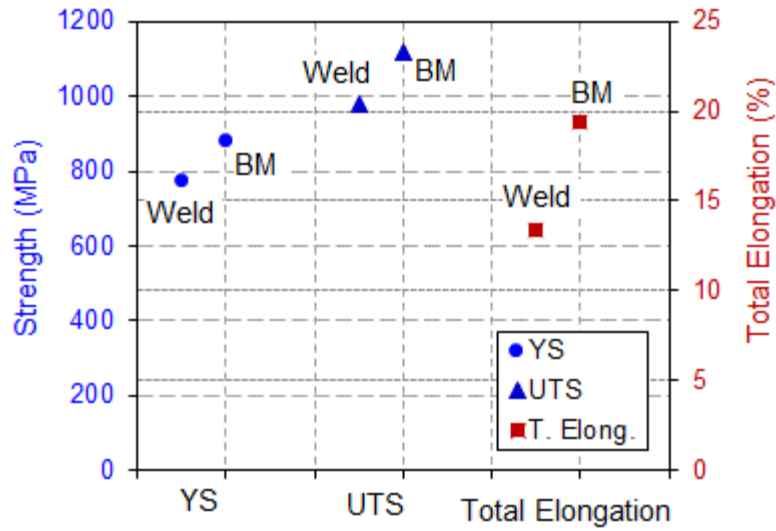
Fig. 3. Average YS, UTS, and total elongation (right hand side vertical axis) of the as-laser welded Ti6242 compared to those of the BM.

Fig. 4. Individual (a) YS, (b) UTS, and (c) total elongation of the three tensile samples extracted from the as-laser welded Ti6242 sheet compared to those of the BM.

(a)
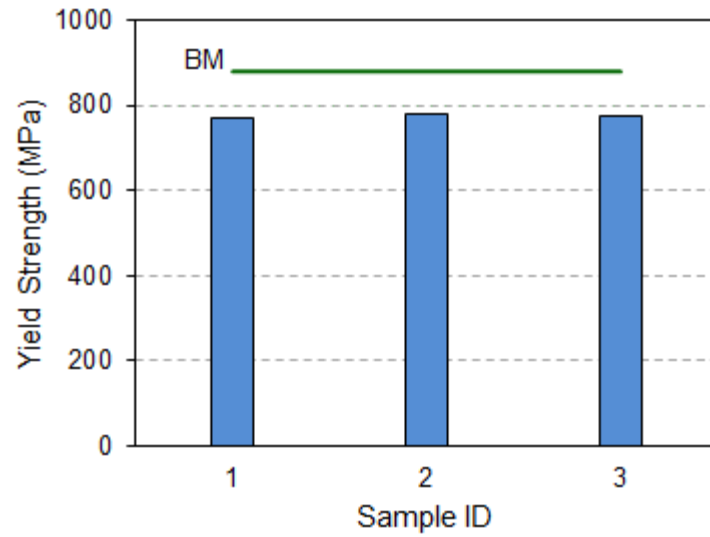
(b)
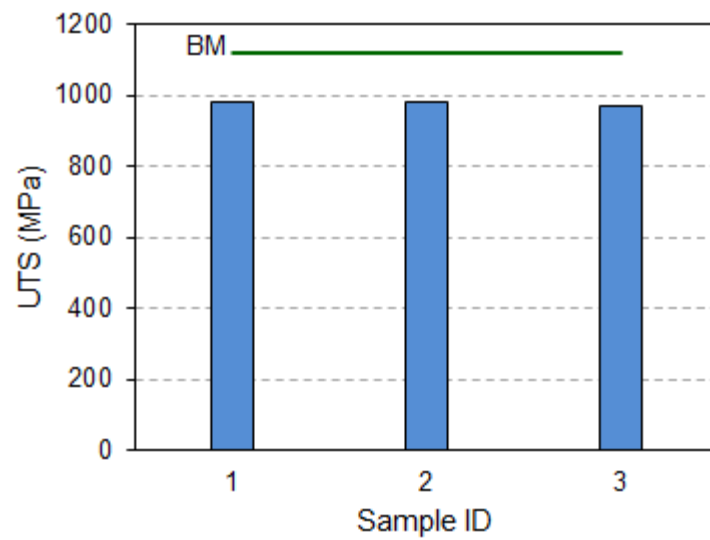
(c)
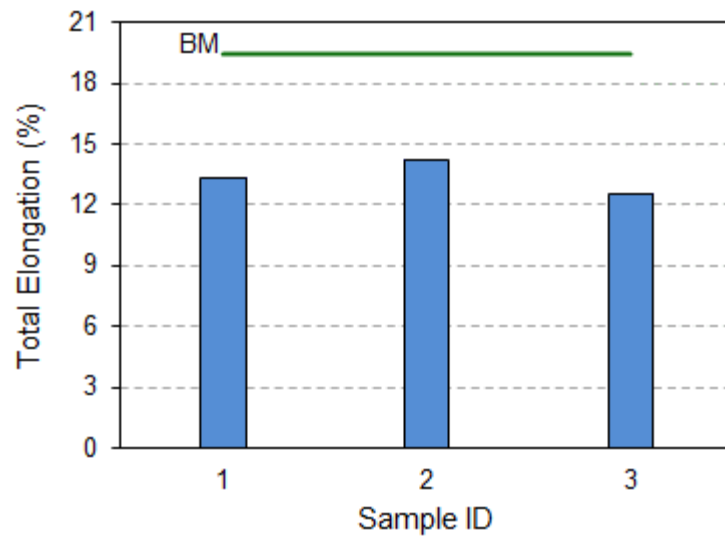
Fig. 4. Individual (a) YS, (b) UTS, and (c) total elongation of the three tensile samples extracted from the as-laser welded Ti6242 sheet compared to those of the BM.

Fig. 5. Typical stress-strain curve of the tensile samples extracted from the as-laser welded Ti6242 sheet compared to that of the BM.
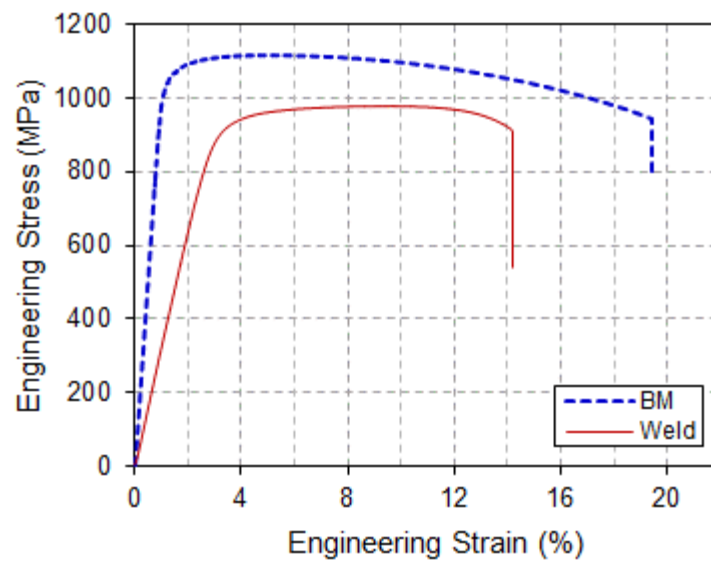
Fig. 5. Typical stress-strain curve of the tensile samples extracted from the as-laser welded Ti6242 sheet compared to that of the BM.

(a)

(b)

(c)

25
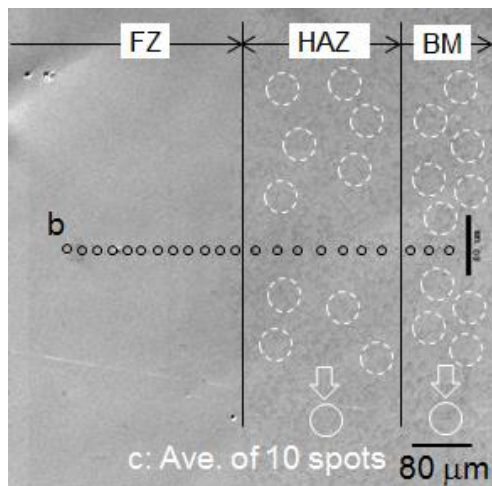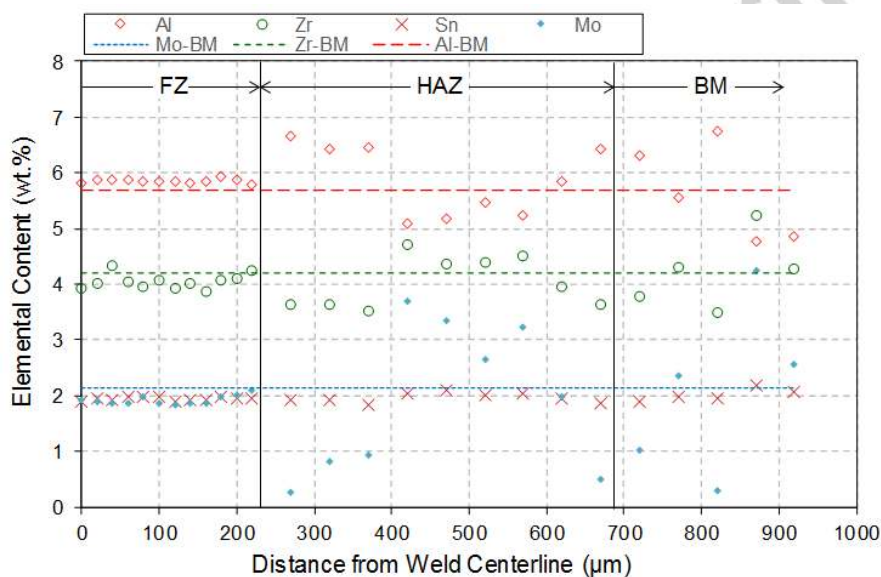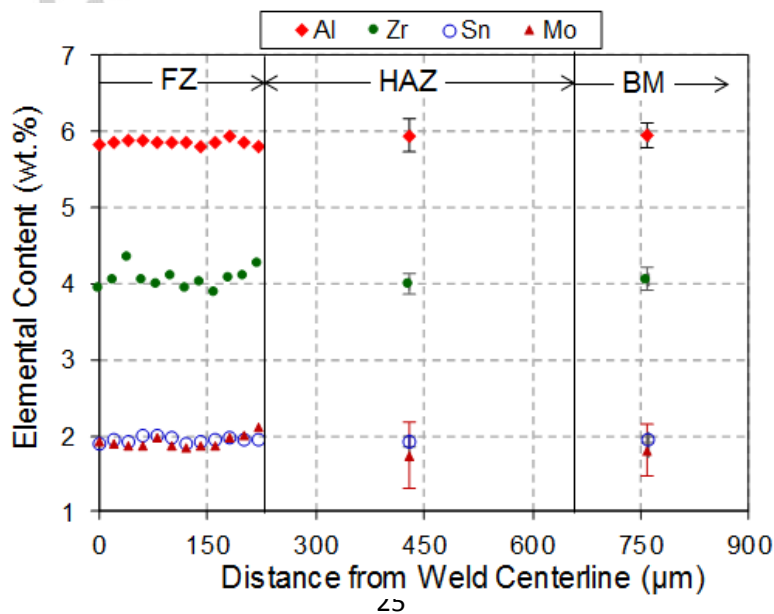
Fig. 6. (a) Schematic showing the EPMA spots across the weld, (b) distribution of the alloying elments across the weld with a EPMA probe size of 2 μm, and (c) average of ten chemical compostion measurments in the HAZ and BM using a spot size of 20 μm comapred to the previous results of the
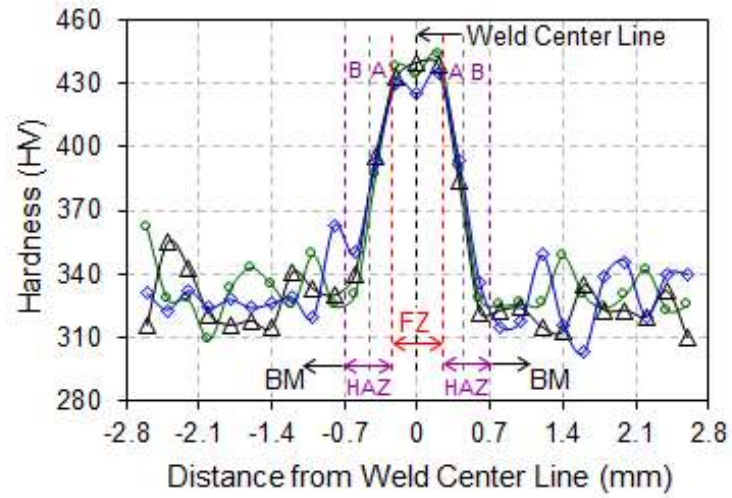
Fig. 7. Microhardness evolution across the weld in laser welded Ti6242. The negative and positive distances from the weld centerline and the three lines for microhardness measurement are depicted schematically in Fig. 2
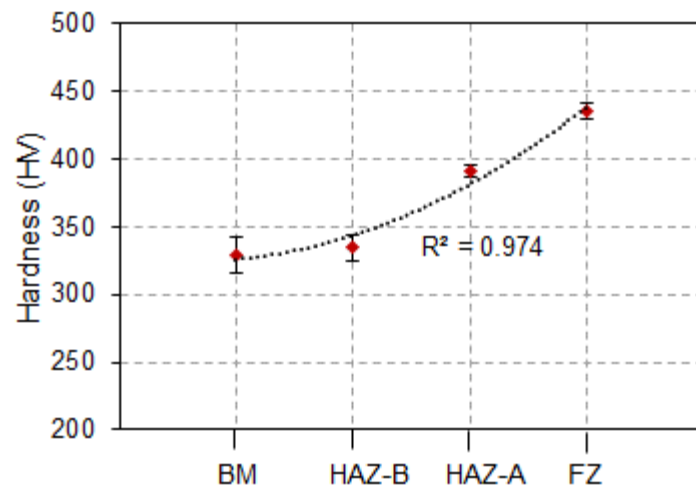
Fig. 8. The average microhardness of the BM, HAZ (subregions A and B), and FZ in laser welded Ti6242. The best fit to the data is depicted as a dotted curve. The standard deviations for the measurements are also shown as error bars.

(a) BM

(b) BM

(c) HAZ

(d) HAZ (region B)

(e) FZ

(f) FZ
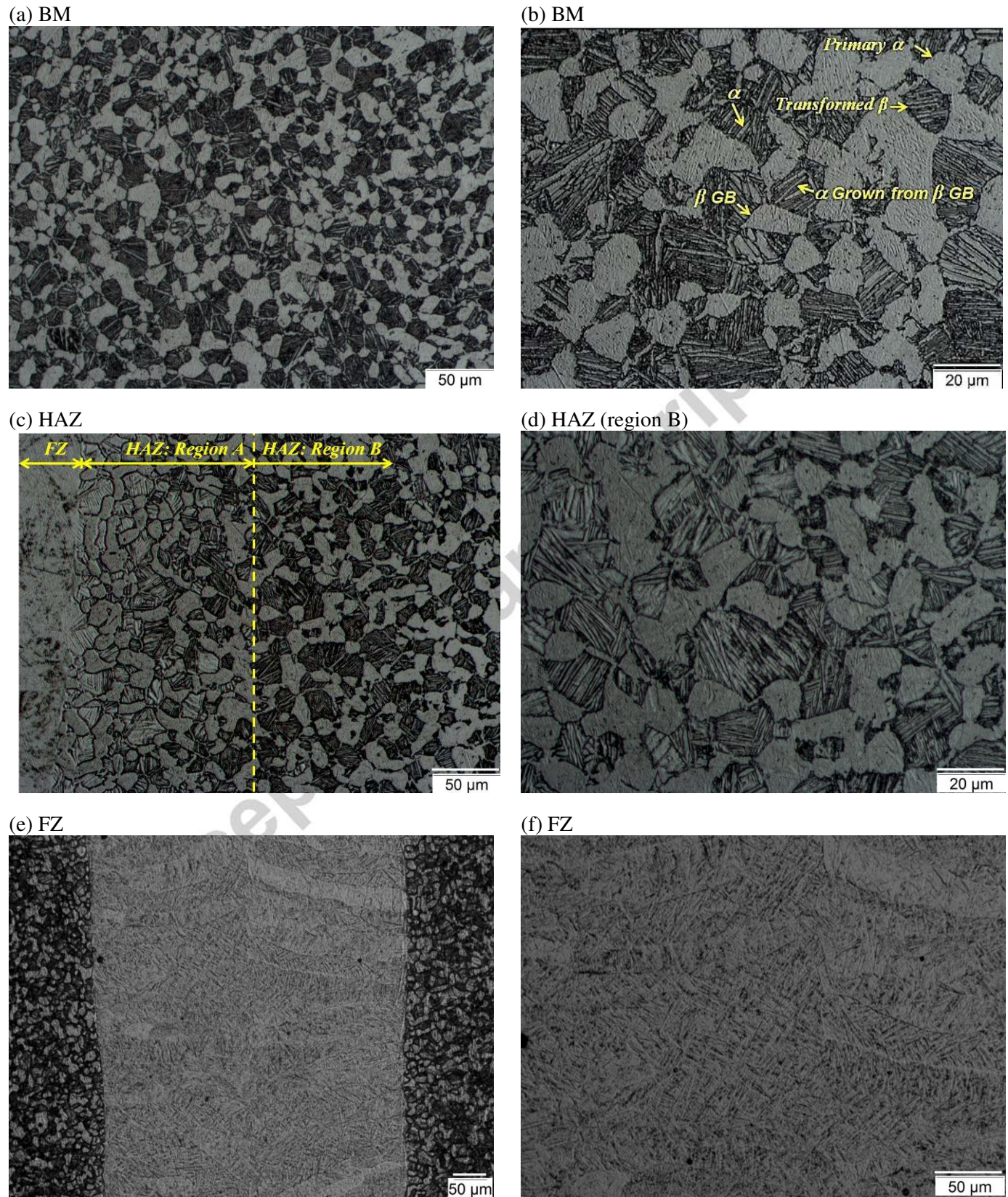
Fig. 9. Optical micrographs showing: (a) and (b) the bimodal microstructure with primary α and transformed β in the forged and annealed as-received BM Ti6242; bright or grey area is α phase and dark area is β, (c) and (d) HAZ microstructure with higher primary α volume fraction in subregion A, (e) and (f) acicular α' martensite formation in the FZ. GB stands for grain boundary.
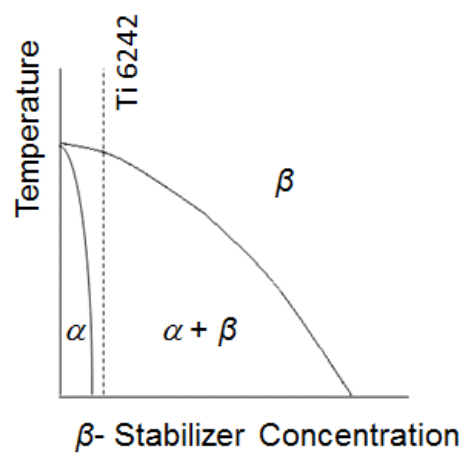
Fig. 10. Location of the Ti6242 alloy in a pseudobinary Ti phase diagram [4].

(a)
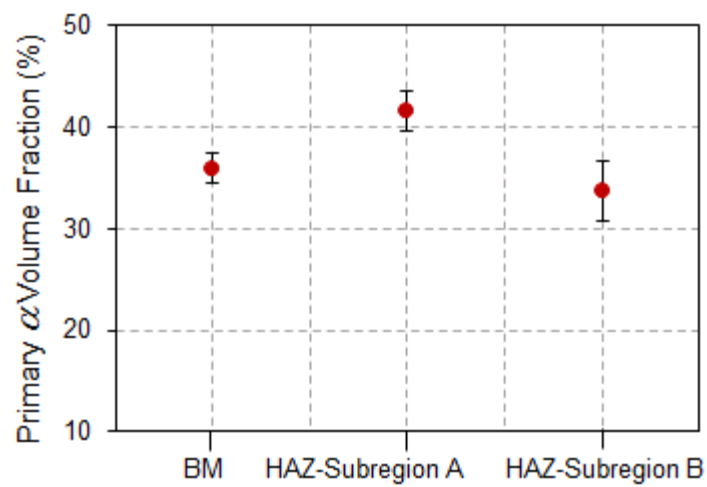
(b)
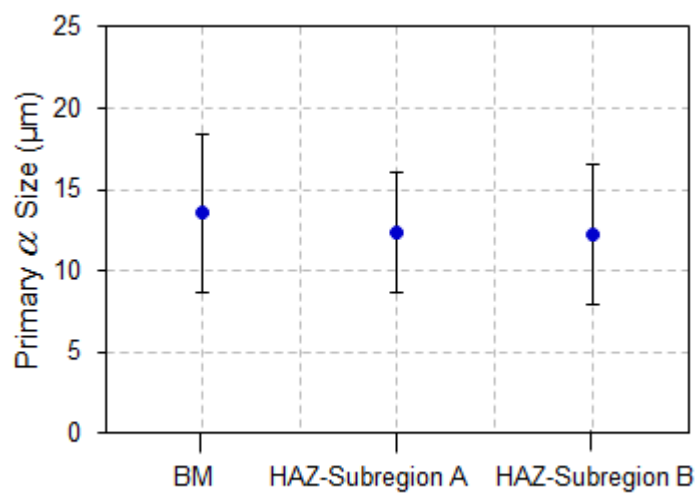
Fig. 11. (a) Volume fraction and (b) size of the primary α in the BM and the two subregions of HAZ in laser welded Ti6242. The standard deviations for the measurements are shown as error bars.
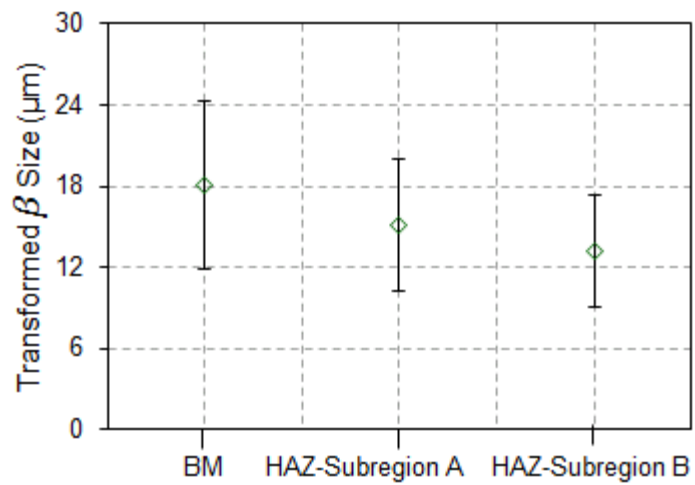
Fig. 12. Size of the transformed β in the BM and two subregions of the HAZ in laser welded Ti6242. The standard deviations for the measurements are shown as error bars.
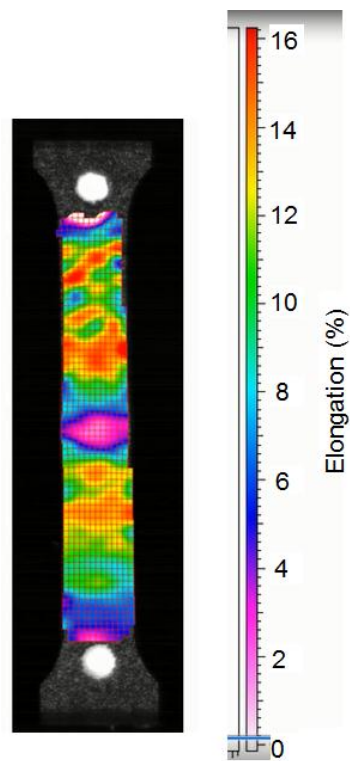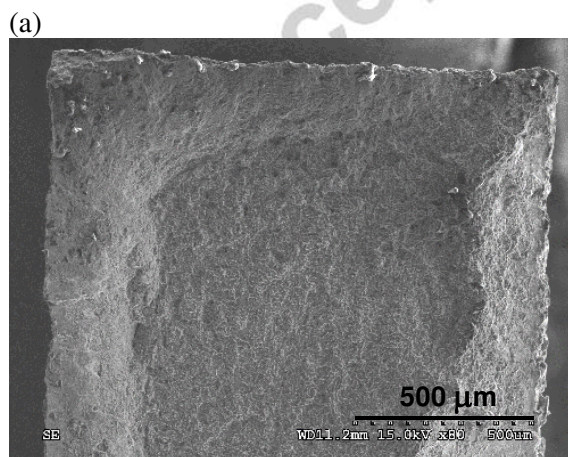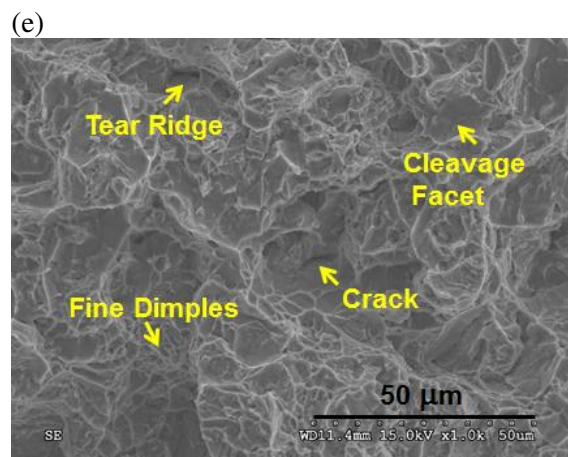
Fig. 13. Distribution of the elongation at the final stages of the tensile test for sample 1 (Fig. 1) extracted from the laser welded Ti6242 sheet.
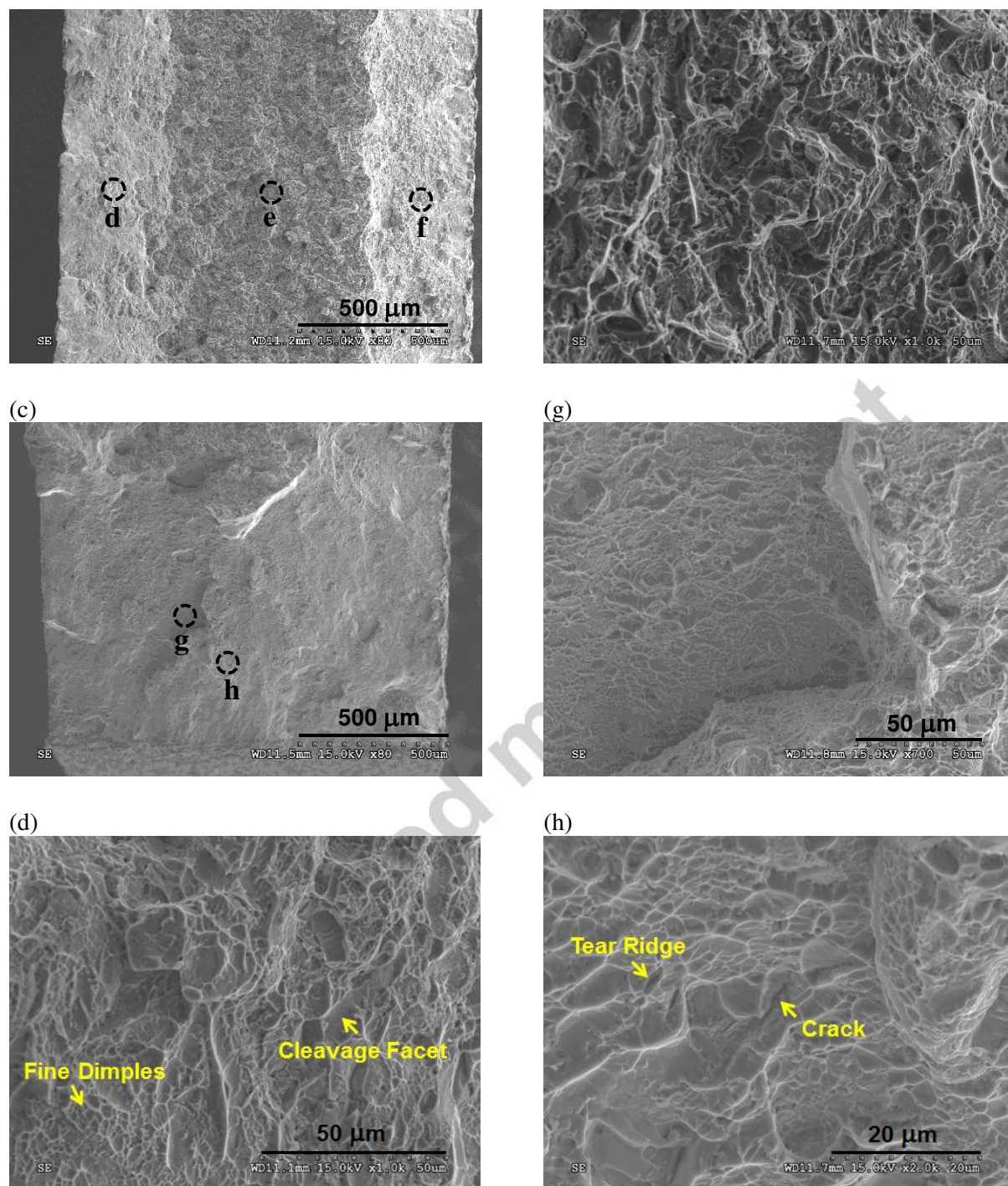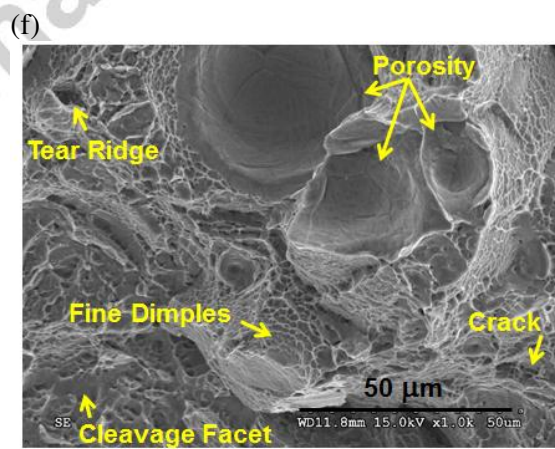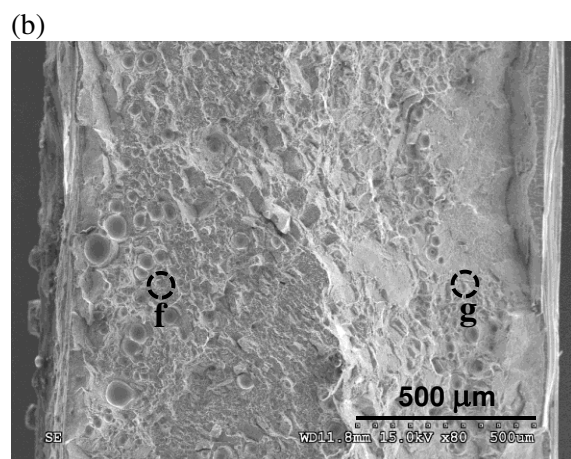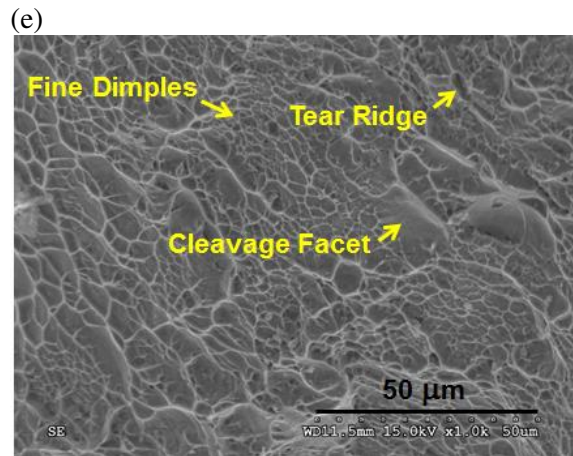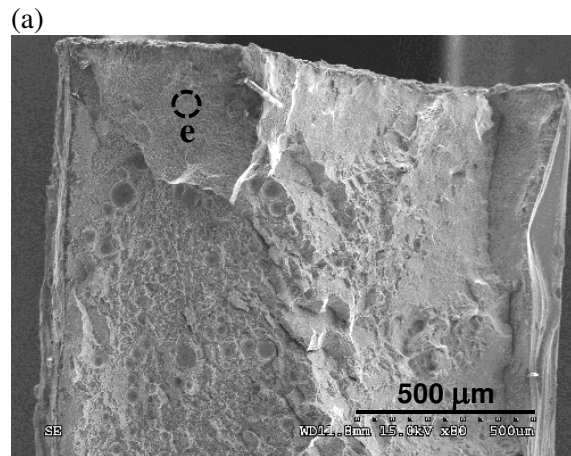
(a)

(e)

(b)

(f)

32

Fig. 14. Fracture surface of the tensile sample 2: (a) to (c) overview, (d) to (h) higher magnification images of the circled areas in b and c.
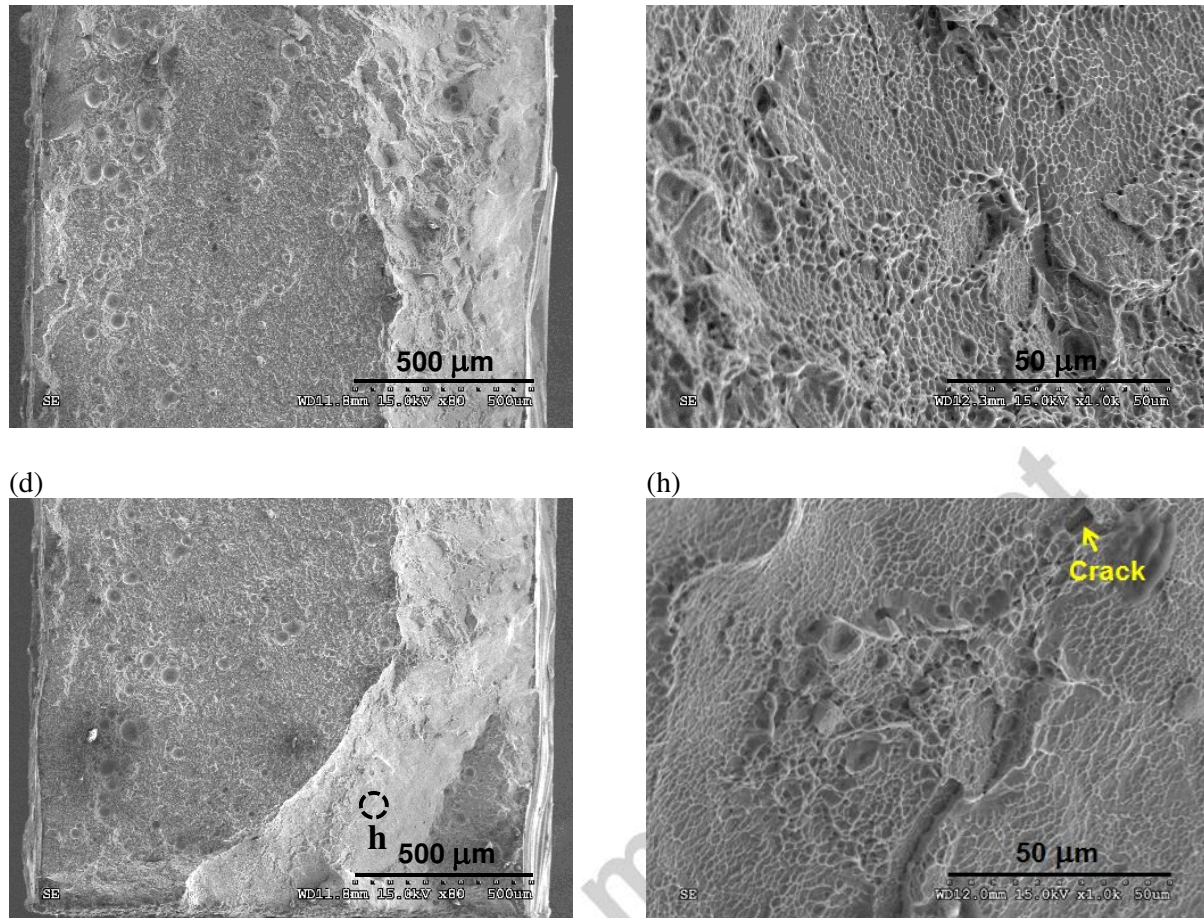
(a)

(b)

(c)

(e)

(f)

(g)

(d)

(h)

Fig. 15. Fracture surface of the tensile sample 3: (a) to (d) overview, (e) to (h) higher magnification images of the circled areas in a, b, and d.

Table 1- Details of grinding and polishing procedures

Grinding/Polishing Surface	Abrasive	Automatic (A)/Manual (M) Grinding/Polishing	Disk/Holder Rotation Speed, rpm	Force per Sample, N	Lubricant	Rotation Direction of Holder Relative to Disk	Time, min
SiC paper	320 grit	A	300/150	40	Water	Same	1
SiC paper	600 grit	A	300/150	40	Water	Same	1
Low nap cloth	6 µm	A	150/150	40	NA	Same	1

35

	diamond						
High nap cloth	1 µm aluminum oxide	M	150/ not applicable (NA)	Firm	NA	NA	1
Medium nap cloth	0.3 µm aluminum oxide	M	150/NA	Firm	NA	NA	2
Medium nap cloth	0.05 µm silicon dioxide	M	150/NA	Firm	NA	NA	2

Table 2- Average tensile properties of the as-laser welded Ti6242 compared to those of the BM

Sample ID	YS, MPa	UTS, MPa	Total Elongation, %	Failure Location
As-laser welded	775 ± 7	977 ± 4	13.4 ± 0.8	Samples 1 and 3 in Fig. 1: FZ, Sample 2: BM
BM	880	1120	19.4	N/A
BM: Reference [13]	895	1018	19.0	N/A